



CHEMISTRY & SUSTAINABILITY

CHEM **SUS** CHEM

ENERGY & MATERIALS

Accepted Article

Title: Structure, activity, and faradaic efficiency of nitrogen-doped porous carbon catalysts for direct electrochemical hydrogen peroxide production

Authors: Yanyan Sun, Shuang Li, Zarko Jovanov, Denis Bernsmeier, Huan Wang, Benjamin Paul, Xingli wang, Stefanie Kuehl, and Peter Strasser

This manuscript has been accepted after peer review and appears as an Accepted Article online prior to editing, proofing, and formal publication of the final Version of Record (VoR). This work is currently citable by using the Digital Object Identifier (DOI) given below. The VoR will be published online in Early View as soon as possible and may be different to this Accepted Article as a result of editing. Readers should obtain the VoR from the journal website shown below when it is published to ensure accuracy of information. The authors are responsible for the content of this Accepted Article.

To be cited as: *ChemSusChem* 10.1002/cssc.201801583

Link to VoR: <http://dx.doi.org/10.1002/cssc.201801583>

WILEY-VCH

www.chemsuschem.org

A Journal of



Structure, activity, and faradaic efficiency of nitrogen-doped porous carbon catalysts for direct electrochemical hydrogen peroxide production

Yanyan Sun,^[a] Shuang Li,^[a] Zarko Jovanov,^[a] Denis Bernsmeier,^[a] Huan Wang,^[a] Benjamin Paul,^[a] Xingli Wang,^[a] Stefanie Kühl,^[a] and Peter Strasser^{*[a]}

Dedication ((optional))

Abstract: Carbon materials doped with nitrogen are active catalysts for the electrochemical two-electron oxygen reduction reaction (ORR) to hydrogen peroxide. Insights into the individual role of the various chemical nitrogen functionalities in the H₂O₂ production, however, have remained scarce. Here, we explore a catalytically very active family of nitrogen-doped porous carbon materials, prepared by direct pyrolysis of ordered mesoporous carbon (CMK-3) with polyethylenimine (PEI). Voltammetric rotating ring-disk analysis in combination with chronoamperometric bulk electrolysis measurements in electrolysis cells demonstrate a pronounced effect of the applied potentials, current densities, and electrolyte pH on the H₂O₂ selectivity and absolute production rates. H₂O₂ selectivity up to 95.3% was achieved in acidic environments, whereas the largest H₂O₂ production rate of 570.1 mmol g⁻¹_{catalyst} h⁻¹ was observed in neutral solution. X-ray photoemission spectroscopy (XPS) analysis suggests a key mechanistic role of pyridinic-N in the catalytic process in acid, while graphitic-N groups appear to be catalytically active moieties in neutral and alkaline conditions. Our results contribute to the understanding and aid the rational design of efficient carbon-based H₂O₂ production catalysts.

The electrochemical oxygen reduction reaction (ORR) is a key reaction for many renewable energy conversion and storage technologies such as rechargeable fuel cells and metal-air batteries.^[1-6] Most catalyst discovery research is focused on four-electron ORR catalysts in order to maximize the energy conversion efficiency of electrochemical energy conversion/storage devices.^[7-12] In contrast, the exploration of two-electron ORR catalysts has long been overlooked, despite the fact that it represents a promising and green route for *in-situ* electrochemical H₂O₂ production.^[13-19] Compared to the state-of-the-art industrial anthraquinone process^[20] or the difficult and potentially unsafe direct catalytic synthesis from hydrogen and oxygen,^[21] electrochemical H₂O₂ production proceeding *via* two-electron oxygen reduction possesses many advantages. These involve simplified and *in-situ* small-scale production, reduced energy input and waste generation, as well as improved process safety compared to method using a direct explosive mixture of hydrogen and oxygen. Moreover, if the two-electron ORR

process is coupled with water electrolyzers powered by renewable power sources, chemical electricity storage is intimately coupled with the production of useful chemicals.^[13] Based on the considerations above, it is of paramount importance to design and synthesize the ORR catalysts with high catalytic activity and faradaic efficiency toward H₂O₂ production.

To date, the proposed alternative ORR catalysts for H₂O₂ production include noble-metal-based alloys,^[15, 17, 22-27] transition-metal oxides/complex,^[28-32] transition-metal/C composites,^[33-35] and metal-free carbon-based materials^[6, 13, 16, 18, 36-38]. Among them, metal-free carbon-based materials proved repeatedly to be the most promising alternative ORR catalysts for H₂O₂ production, largely due to their low-cost, facile preparation, favorable selectivity, and strong chemical stability. Considerable efforts have been devoted to the design and screening of a variety of nanostructured carbon-based materials with different heteroatoms such as nitrogen or sulfur. More specifically, nitrogen-doped porous carbon materials have received the most attention recently, owing to their high specific surface area and electronic conductivity, good catalytic activity and durability. To date, reported synthetic strategies toward nitrogen-doped porous carbon materials were twofold: (1) the direct synthesis in the presence of carbon and nitrogen sources *via* pyrolysis,^[11, 18, 39-40] chemical vapor deposition,^[41] or the newly developed electrochemical doping;^[42] (2) nanocasting strategy using commercial SiO₂ as sacrificial hard template with subsequent pyrolysis.^[38, 43-44] Although some promising results have been achieved, there is plenty room for improvement in terms of selectivity. On one hand, the activity and faradaic efficiency of the H₂O₂ producing catalysts have remained too low for commercialization and need further improvement before developing practically viable devices. On the other hand, there are a number of important fundamental aspects about the H₂O₂ formation process that have remained elusive: for instance, the understanding of the catalytically active sites has remained unclear, in part owing to the inevitable co-generation and co-existence of chemically distinct nitrogen species (N-functionalities) within the resultant nitrogen-doped carbon materials and the lack of their direct experimental observations.^[1-2, 45] To remedy this, more controlled synthesis methods are needed where only one type of N-functionality forms in order to establish structure-selectivity relationships; or else, analysis techniques are required that allow deconvolution of the contributions of the chemically distinct N-functionalities and their carbon environment in parallel. Once the catalytically active site or chemical motif is identified, this would prompt synthetic efforts to maximize their population (maximizing the

[a] Yanyan Sun, Shuang Li, Dr. Zarko Jovanov, Dr. Denis Bernsmeier, Dr. Huan Wang, Benjamin Paul, Xingli Wang, Dr. Stefanie Kühl, Prof. Peter Strasser.
Department of Chemistry, Chemical Engineering Division,
Technical University of Berlin, 10623 Berlin, Germany
E-mail: pstrasser@tu-berlin.de

Supporting information for this article is given via a link at the end of the document. ((Please delete this text if not appropriate))

active site density), which would boost H_2O_2 production activity and faradaic efficiency.

In the present work, we have developed a facile synthetic method for preparing porous nitrogen-doped carbon catalysts. We investigated the effect of applied potentials and electrolyte pH on the H_2O_2 selectivity and absolute H_2O_2 production yields by means of the rotating ring-disk electrode (RRDE) and chronoamperometric bulk electrolysis tests at stationary planar electrodes. In order to link the catalytic rates and efficiencies to chemical and morphological structure of the catalysts in different electrolytes, a detailed chemical speciation of nitrogen functionalities before and after the catalysis was conducted by x-ray photoemission spectroscopy (XPS).

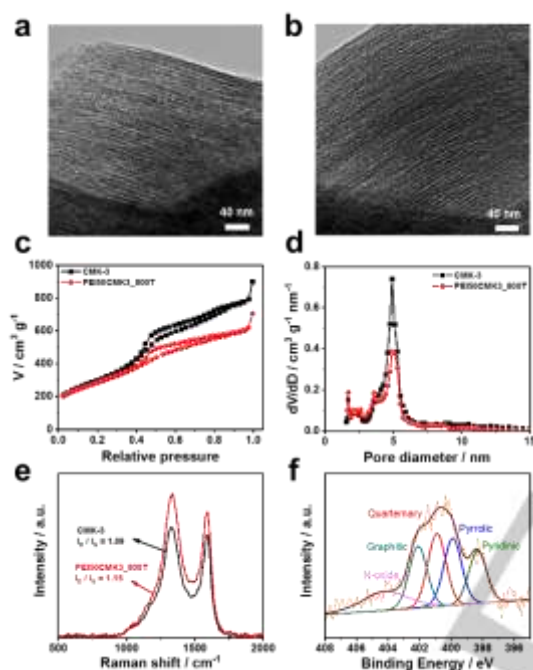


Figure 1. TEM images of (a) CMK-3 and (b) PEI50CMK3_800T; (c) N_2 adsorption isotherms, (d) pore size distribution and (e) Raman spectra of CMK-3 and PEI50CMK3_800T with their characteristic D/G band intensity ratios; (f) the deconvolution of the N 1s spectra of PEI50CMK3_800T with different N species as shown.

The nitrogen-doped porous carbon catalysts were prepared by ultrasonically mixing ordered mesoporous carbons (CMK-3) with calculated amounts of polyethylenimine (PEI) followed by annealing in N_2 atmosphere. Here PEI is chosen as nitrogen precursor mainly due to its low-cost and high nitrogen content up to 32.5%. A typical synthetic recipe involves mixing the CMK-3 carbon precursor with 50 μL PEI aqueous solution (30% w/v) followed by annealing at 800 $^\circ\text{C}$ (the resulting catalyst will henceforth be denoted as PEI50CMK3_800T). The morphologies of CMK-3 and PEI50CMK3_800T were first characterized by transmission electron microscopy (TEM), as shown in **Figure 1a-b**. After nitrogen doping, the ordered porous structure was well retained, thereby facilitating oxygen mass transport during the H_2O_2 production process. During the formation process of nitrogen-doped carbon, PEI filled the pores of CMK-3 owing to capillary siphons and then carbonization

occurred, forming chemical nitrogen-doped carbon functionalities of CMK-3. The porous properties and Brunauer-Emmett-Teller (BET) surface areas were then evaluated by nitrogen adsorption-desorption isotherms. An obvious hysteresis loop at relative pressure range between 0.4 and 0.8 and a narrow pore size distribution centered around 5 nm for both CMK-3 and PEI50CMK3_800T can be observed (**Figure 1c and d**), confirming the mesoporous structures. In addition, similar phenomenon was also observed for other nitrogen-doped carbon materials prepared at different conditions (**Figure S1**). An exception was the sample prepared at 900 $^\circ\text{C}$ demonstrating a certain degree of microporous structure. Moreover, all nitrogen-doped carbon catalysts retained extremely high Brunauer-Emmett-Teller (BET) surface areas from 726 to 1682 $\text{m}^2 \text{g}^{-1}$, which were beneficial for exposing more catalytically active sites and improved mass transport during the ORR process.^[37, 44, 46]

The crystallinity of nitrogen-doped porous carbon catalysts was investigated by powder X-ray diffraction (PXRD). For CMK-3, there are two major diffraction peaks at 30.2 $^\circ$ and 42.9 $^\circ$ (**Figure S2a**), which can be ascribed to be the (002) and (101) crystal planes of graphite. Interestingly, after acid-treatment and nitrogen doping, the characteristic interlayer (002) diffraction peak shifted down to around 24 $^\circ$, indicating an expanded interlayer distance.^[13] All catalysts exhibited a broad diffraction peak revealing characteristic features of amorphous carbon (**Figure S2**). Raman spectroscopy was carried out to assess the graphitization degree and defect content in nitrogen-doped carbon catalysts. To achieve this, we evaluated peaks at 1330 cm^{-1} and 1585 cm^{-1} for all catalysts (**Figure 1e and Figure S3**), which are attributed to D and G band of carbon materials, respectively. Generally, the intensity ratio of the D band to G band (I_D/I_G) is a qualitative estimate of the defect content in the doped carbon, since the D and G bands are related to disordered and ordered crystalline sp^2 carbon domains, respectively.^[13] Pyrolytic nitrogen doping led to slightly increased I_D/I_G values, implying an increase in structural disorder and defects. Besides, the slight downshifts of the G band after pyrolytic nitrogen doping suggest that doping altered both the crystallinity and the electronic structure of carbon nanostructures likely due to a reduction in the mean sheet width of un-doped graphene.^[47-48]

X-ray photoelectron spectroscopy (XPS) was also performed to analyze the surface composition and electronic states of the nitrogen-doped carbon materials. **Figure 1f** shows the high-resolution N 1s spectra of the nitrogen-doped carbon catalysts, which can be further divided into five peaks assigned to different nitrogen species including pyridinic-N (398.3 eV), pyrrolic-N (399.9 eV), quaternary-N (400.9 eV), graphitic-N (402.1 eV), and N-oxide (404.1 eV).^[49-52] The detailed content of carbon and nitrogen, and different nitrogen species are summarized in **Table S1** and **Table S2**. The variations in the N content of the resultant catalysts are consistent with that examined results from element analysis (EA) (**Table S3**), indicating that the nitrogen dopant amount can be tuned within the range from 0.07% to 2.04%.

The electrochemical activity and selectivity of the nitrogen-doped porous carbon catalysts toward ORR to H_2O_2 production was evaluated using a three-electrode rotating ring-disk electrode

(RRDE) techniques. Unlike pristine CMK-3, the N-modified PEI50CMK3_800T catalyst exhibited relatively positive onset potential, significantly increased disk currents and ring current at the investigated range of applied potential (**Figure 2a**), which was also observed for the other nitrogen-doped carbon catalysts prepared at different conditions (**Figure S4a and Figure S5a**). This demonstrates that nitrogen doping resulted in an enhanced oxygen reduction activity coupled with improved H₂O₂ selectivity. Quantitative H₂O₂ selectivities (in %) and the number of electrons transferred during the ORR process were evaluated, as well (**Figure 2b, Figure S4b and Figure S5b**). After nitrogen doping, the H₂O₂ selectivity improved sharply from 77.2% to 97.4%, and the corresponding averaged number of electrons transferred per oxygen molecule decreased from 2.46 to 2.05 at +0.3 V_{RHE}, close to the theoretical value of 2 for H₂O₂ selectivity. In particular, the PEI50CMK3_800T catalyst achieved the highest H₂O₂ selectivity of 95.2%–98.5% within the potential range from +0.1 to +0.4 V_{RHE}, which outperformed previously reported nitrogen-doped carbon^[37–40] and noble-metal-based alloys catalysts (**Table S4**).^[15, 17, 22–25, 53]

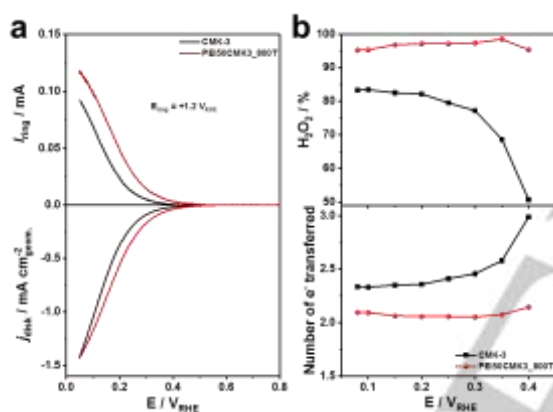


Figure 2. (a) Linear sweep voltammetry performed by a rotating ring-disk electrode (RRDE) technique where the ring current is collected on the Pt ring at a constant potential of 1.2 V_{RHE}, and (b) calculated H₂O₂ selectivity (%) and the number of electron transferred (n) as a function of electrode potential for two materials: CMK-3 and PEI50CMK3_800T. In all cases, measurements were performed in O₂-saturated 0.5 M H₂SO₄ at a scan rate of 5 mV s⁻¹ with 1600 rpm at room temperature and the catalyst loading amount was set to 0.05 mg cm⁻².

In addition to the optimization of catalyst preparation, we studied the effects of electrolyte pH on electrochemical H₂O₂ production of the PEI50CMK3_800T catalyst (**Figure 3**). As shown in **Figure 3a**, the onset potential (defined as potential at the current density of 0.01 mA cm⁻²)^[54] of oxygen reduction decreased in the order of KOH (0.84 V_{RHE}) > K₂SO₄ (0.52 V_{RHE}) > H₂SO₄ (0.49 V_{RHE}) with the highest oxygen transport-limited disk current and ring current obtained in 0.1 M KOH. In alkaline condition, the Pt ring current exhibited a maximum HO₂⁻ production at +0.5 V_{RHE} of disk potential, below which the HO₂⁻ production decreased gradually with negative shift of disk potentials. The effect of the nature of the electrolyte on the H₂O₂ selectivity is shown in **Figure 3b**. The highest H₂O₂ selectivity was observed in 0.5 M H₂SO₄, and decreased in the order of H₂SO₄ (98.5%) > K₂SO₄

(89.8%) > KOH (83%) at +0.35 V_{RHE} of disk potential. This trend is rationalized by the establishment of the parallel 4-electron pathway at smaller potentials.

Tafel plots were evaluated from the experimental RRDE data in different electrolytes to verify the influence of pH on ORR mechanism (**Figure 3c**). Here the kinetic current densities ($j_{disk, kin}$) can be calculated according to the Koutecky–Levich equation:

$$1/j_{disk} = 1/j_{disk, kin} + 1/j_{disk, lim} \quad (1)$$

where j_{disk} and $j_{disk, lim}$ are the measured current density and the diffusion-limited current density, respectively.^[35] Besides, $j_{disk, lim}$ can be obtained using the Levich equation:

$$j_{disk, lim} = 0.62nFD^{2/3}v^{-1/6}\omega^{1/2}C \quad (2)$$

where C, F, D, n, v, and ω refer to the bulk concentration of oxygen (1.2 × 10⁻⁶ mol cm⁻³ for pH 5–13 and 1.1 × 10⁻⁶ mol cm⁻³ for pH 0.3), Faraday constant (96485 C mol⁻¹), the diffusion coefficient of oxygen (1.9 × 10⁻⁵ cm² s⁻¹ for pH 5–13 and 1.8 × 10⁻⁵ cm² s⁻¹ for pH 0.3), the number of electrons transferred, the kinetic viscosity (0.01 cm² s⁻¹) and the angular velocity of the disk ($\omega = 2\pi N$, N is the linear rotation speed).^[35, 55–57] The corresponding Tafel slopes can be calculated to be 161.3 mV dec⁻¹ for pH 0.3, 95.7 mV dec⁻¹ for pH 7.0, and 67.5 mV dec⁻¹ for pH 13.0, respectively, which are in accordance with the previously reported values for nitrogen-doped carbon-based ORR catalysts.^[18] These results demonstrate that the ORR mechanism on the evaluated catalysts exhibits strong pH-dependence, which affects the overall activity and selectivity for peroxide production.

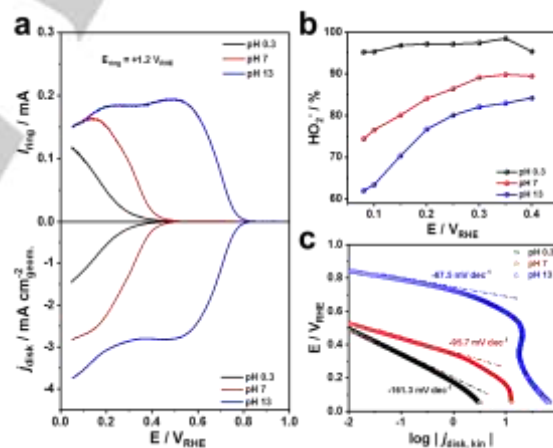


Figure 3. Electrochemical measurement of the optimized sample PEI50CMK3_800T in different electrolytes: (a) linear sweep voltammetry of RRDE measurement with ring current collected on the Pt ring at a constant potential of 1.2 V_{RHE}, and the disk geometric current density (geometric area is 0.2475 cm²), (b) H₂O₂ selectivity (%), and (c) Tafel plots. Note: the measurement was conducted in O₂-saturated 0.5 M H₂SO₄ (pH=0.3), 0.1 M K₂SO₄ (pH=7), and 0.1 M KOH (pH=13) at a scan rate of 5 mV s⁻¹ with 1600 rpm at room temperature and the catalyst loading amount is 0.05 mg cm⁻².

To evaluate the H₂O₂ production of the N-modified carbons over extended periods of time, bulk electrolysis tests were conducted in a custom-made two-chamber H-Cell with different electrolytes including 0.5 M H₂SO₄ (pH=0.3), 0.1 M K₂SO₄ (pH=7), and 0.1 M KOH (pH=13), whereby H₂O₂ concentration was determined

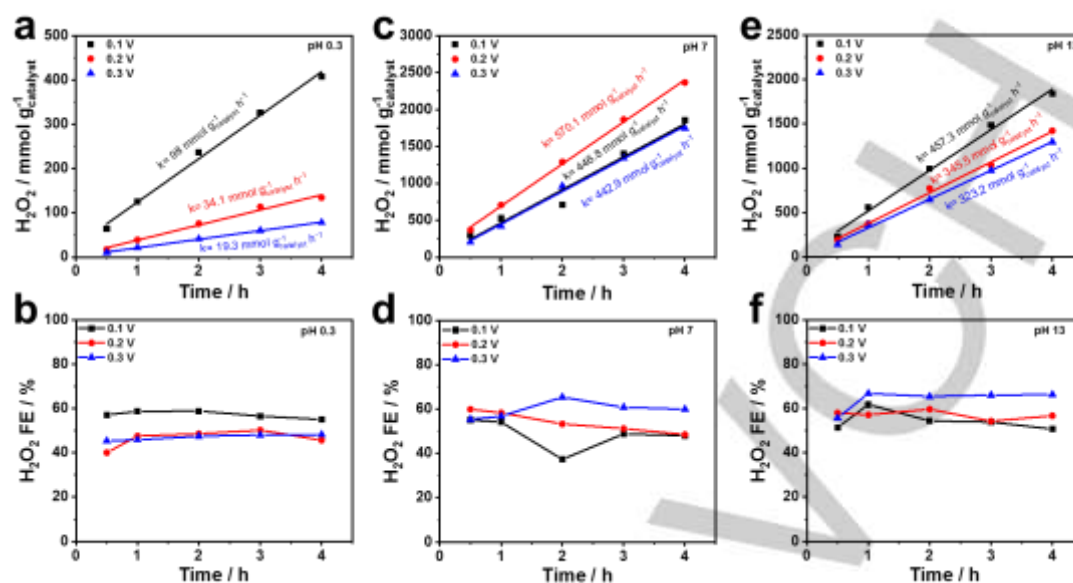


Figure 4. (a, c, e) H_2O_2 production amount normalized by catalyst loading amount over the reaction time, and (b, d, f) faradaic H_2O_2 efficiency (FE) of PEI50CMK3_800T catalysts in O_2 -saturated 0.5 M H_2SO_4 (pH=0.3) (a, b), 0.1 M K_2SO_4 (pH=7) (c, d), and 0.1 M KOH (pH=13) (e, f).

using UV-Vis absorption spectrometry. **Figure 4a, c, e** plot the potentiostatic H_2O_2 production normalized by the catalyst loading over the reaction time at different applied potential of +0.3, +0.2, and +0.1 V_{RHE} . As shown, the H_2O_2 production rates increased with negative shift of applied potential in both acidic and alkaline solutions. In neutral conditions, the optimal applied electrode potential was +0.2 V_{RHE} . The H_2O_2 production rate at +0.2 V_{RHE} decreased in the order of K_2SO_4 ($570.1 \text{ mmol g}_{\text{catalyst}}^{-1} \text{ h}^{-1}$) > KOH ($345.5 \text{ mmol g}_{\text{catalyst}}^{-1} \text{ h}^{-1}$) > H_2SO_4 ($34.1 \text{ mmol g}_{\text{catalyst}}^{-1} \text{ h}^{-1}$), indicating that the pH has a significant effect on the H_2O_2 production. **Figure 4b, d, f**, report the faradaic H_2O_2 efficiency: good faradaic H_2O_2 efficiencies of 40%-59% were observed in 0.5 M H_2SO_4 (pH=0.3), higher values of 37%-65% were obtained in 0.1 M K_2SO_4 (pH=7), while somewhat higher values of 51%-67% were measured 0.1 M KOH (pH=13). Clearly, the long-term faradaic H_2O_2 efficiency differed significantly from the H_2O_2 selectivity obtained from voltammetric scans of the RRDE method.

The difference between long-term faradaic H_2O_2 efficiency and the RRDE-derived H_2O_2 selectivity is likely due to the longer residence times of H_2O_2 during bulk electrolysis, resulting in its gradual chemical decomposition *via* disproportionation ($H_2O_2 \rightarrow H_2O + \frac{1}{2} O_2$) or further electrochemical reduction ($H_2O_2 + 2H^+ + 2e^- \rightarrow 2H_2O$).^[24] To validate this hypothesis, the chemical disproportionation and electrochemical reduction of H_2O_2 were carried out and studied on the PEI50CMK3_800T catalyst in the different electrolyte containing $2.5 \text{ mg L}^{-1} H_2O_2$ and $1 \text{ mM } H_2O_2$, respectively (**Figure S6**). As expected, disproportionation of H_2O_2 was observed in alkaline solution, whereas little to no H_2O_2 chemical decomposition was observed in acidic and neutral solutions (**Figure S6a**). Also, the PEI50CMK3_800T catalyst exhibited the electrochemical activity toward H_2O_2 reduction in

neutral and alkaline solutions whereas no obvious electrochemical reduction could be detected in acidic solution (**Figure S6b**). In all, the PEI50CMK3_800T catalyst displayed excellent electrochemical stability at different applied potentials over a wide range of pH values during the successive electrochemical H_2O_2 production within 4 hours (**Figure S7**). These results demonstrated that the PEI50CMK3_800T catalyst is a very promising and efficient catalyst for the electrochemical H_2O_2 production.

In order to gain more insight into the chemical stability and possibly related mechanistic roles of the different chemical states of nitrogen during the 2-electron oxygen reduction process, we investigated the quantitative changes in the chemical nitrogen species before and after the catalysis using XPS. **Figure 5a-d** illustrates the XPS peak analysis of the various N-functionalities before and after the catalysis at pH=0.3, pH=7, and pH=13. The changes of N types after reaction are found to be dependent on the electrolyte pH since significant different changes in the pyridinic-N and graphitic-N contents before and after the catalysis are observed in acidic, neutral, and alkaline solutions (**Table 1**). In acidic condition, pyridinic-N content decreased, while graphitic-N slightly increased. In neutral and alkaline solutions, the opposite is observed: the pyridinic-N content slightly increased, while the graphitic-N content decreased. Furthermore, pyrrolic nitrogen is generally known to be more sensitive to oxidation than the pyridinic-N and graphitic-N during the ORR process.^[45] This is why generally lower pyrrolic-N content is expected after the catalysis. However, the experiments revealed that the pyrrolic-N content actually increased after the catalysis in acidic, neutral, and alkaline solutions.

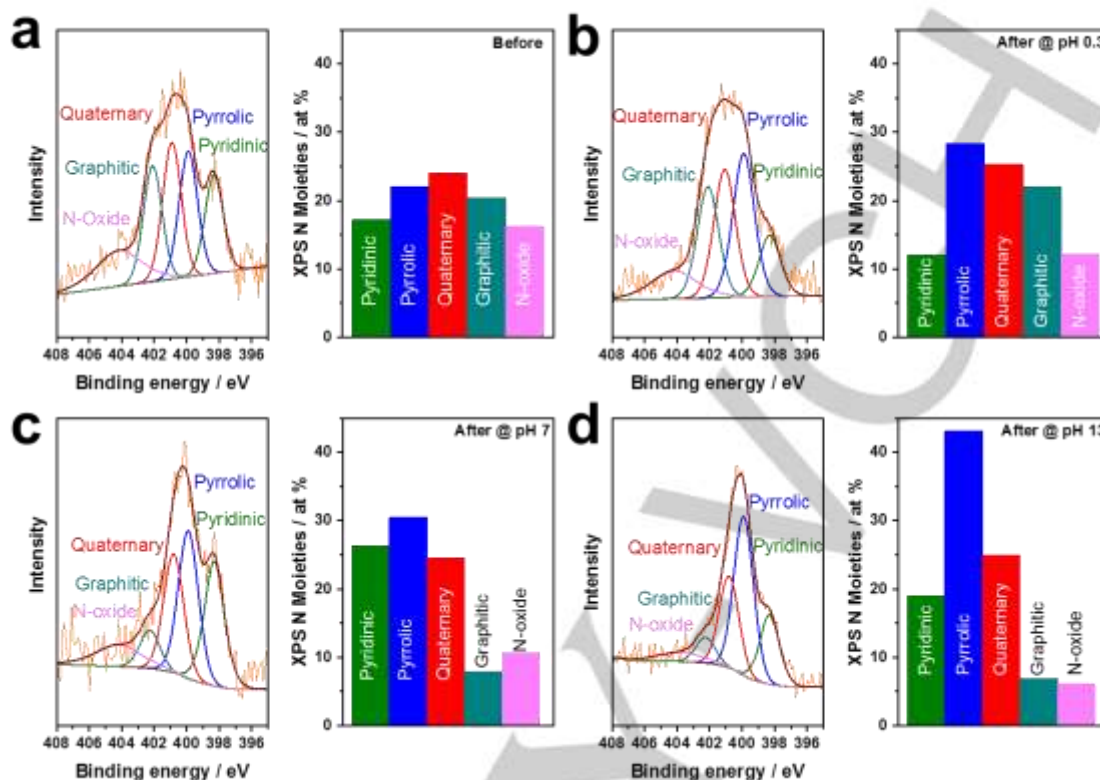


Figure 5. (a-d) The relative content change of various nitrogen species of the PEI50CMK3_800T catalysts before (a) and after the catalysis in (b) pH=0.3, (c) pH=7, and d) pH=13.

Table 1. The nitrogen species change of PEI50CMK3_800T before and after the catalysis in different electrolytes including 0.5 M H₂SO₄, 0.1 M K₂SO₄, and 0.1 M KOH.

N species	Before (%)	Acid (%)	Neutral (%)	Alkaline (%)
Pyridinic-N	17.2	12.13	26.37	18.95
Pyrrolic-N	22.09	28.39	30.49	43.12
Quaternary-N	24.12	25.28	24.59	24.92
Graphitic-N	20.35	22.01	7.86	6.92
N-oxide	16.23	12.19	10.68	6.09

To rationalize the changes in the relative content of the N species consistently, we look at the concomitant changes in their chemical environment during the ORR process in more detail. Recent work has revealed that during oxygen reduction adsorbed oxygenated intermediates, such as O_{ads} or OH_{ads}, may also chemically modify the immediate chemical environment of the catalytically active site or structural motif of the catalysts.^[1, 45, 58] With the covalent attachment of an OH group to the carbon atoms neighboring a pyridinic N, a pyridonic N species is formed (Figure S9), the N 1s binding energy of which was reported to upshift to 400.2 eV from the starting pyridinic N energy of 398.8 eV, which is actually very close to the conventionally reported

binding energy of pyrrolic-N.^[1, 45] This is why we believe that the decrease in pyridinic-N content coupled with the unexpected increase in pyrrolic-N content after the catalysis in acidic solution is rather due to the conversion of pristine pyridinic-N to pyridonic-N than due to a rearrangement of the N atoms.^[45] In contrast, the attachment of –OH to the carbon atoms next to graphitic-N was reported to result in the downshift of nitrogen binding energy to around 400 eV, which again coincides with the typically reported binding energy of pyrrolic-N.^[58] This offers a plausible explanation for the decrease in graphitic-N and increase in pyrrolic-N in neutral and alkaline solutions. This hypothesis further implies that pyridinic-N has a critical role as a catalytically active site in acidic solution, whereas graphitic-N is more likely the catalytically active site in neutral and alkaline solutions. In other words, pyridinic-N does the catalysis in acidic solution, whereas graphitic-N plays an important role in neutral and alkaline solutions.

In conclusion, nitrogen-doped porous carbon catalysts were prepared by direct pyrolysis of CMK-3 and PEI. RRDE results and chronoamperometric bulk electrolysis measurements demonstrated that the pH of the electrolytes and applied potentials have a pronounced effects on the H₂O₂ selectivity and production rate over the optimal nitrogen-doped porous carbon catalysts. In acidic solution, the highest H₂O₂ selectivity of 95.3% at 0.1 V_{RHE} can be achieved whereas in neutral solution the

highest H₂O₂ production rate of 570.1 mmol g⁻¹_{catalyst} h⁻¹ can be obtained. Analyses of the chemical state trajectories of nitrogen in the carbon catalysts suggest a significant role of pyridinic-N in the catalytic process in acid, while graphitic-N groups appear to be catalytically active moieties in neutral and alkaline conditions. Our results contribute to our understanding of carbon-based H₂O₂ production catalysts and also aid the rational design thereof.

Experimental Section

Chemicals

CMK-3 was purchased from East High Tech Limited. Polyethylenimine (PEI) was obtained from Sigma-Aldrich. Hydrogen peroxide test kits were acquired from Merck. All chemicals were used without further treatment.

Synthesis of nitrogen-doped mesoporous carbon

CMK-3 was firstly pre-treated in 2.4 M HNO₃ for 12 h, and dried at 100 °C. Then 30 mg acid-treated CMK-3 with different amount of PEI (25, 50, 100 μL) were dispersed in 2.5 mL of deionized water with the assistance of grinding. The resultant mixture was annealed in a quartz furnace under a continuous flow of nitrogen gas according to the following procedure: firstly heated to 180 °C for 2 h, and then heated to different annealing temperature (600, 700, 800 and 900 °C) for 4 h with the rate of 5 °C min⁻¹. For simplicity, the resultant N-doped CMK-3 samples were labelled as PEIXCMK3_YT (with X the PEI in microliters and Y the annealing temperature in degrees Celsius).

Structural and composition characterization

Powder X-ray diffraction (PXRD) patterns were performed on a Bruker D8 Advance instrument with Cu K_α radiation (λ = 1.54056 Å) in the range from 10° to 90°. Brunauer-Emmett-Teller (BET) surface area was measured with Quantachrome Autosorb-1-C equipment, and pore size distribution can be obtained from the adsorption branches of the isotherms according to cylindrical pores non-localized density functional theory. The morphologies and structures of the catalysts were analyzed by transmission electron microscopy (TEM, FEI Tecnai G² 20 S-TWIN). TEM samples were prepared by dispersing the resultant PEIXCMK3_YT into ethanol solution and then dropping onto the surface of Cu grid, finally drying in the oven at 60 °C for several minutes. The element analysis of the catalysts including C, H, and N contents were conducted with a CHN elemental analyzer (Perkin-Elmer, Model 2400-II). X-ray photoelectron spectra (XPS) were determined by an X-ray photoelectron spectrometer (K-Alpha™, Thermo Scientific). Raman spectra measurement was obtained on a Bruker SENTERRA Raman system.

Electrochemical characterization

The oxygen reduction performances of the resultant catalysts were evaluated in home-made electrochemical cell with three-electrode configuration including the rotating-ring disk electrode (RRDE, PINE Research Instrumentation, 0.2475 cm²), Pt mesh, and a mercury/mercurous sulfate electrode (MMS, PAR / AMETEK USA, calibration against a reversible hydrogen electrode in 0.5 M H₂SO₄ resulted in a reference electrode potential of +0.704 V_{RHE}) as working, counter, and reference electrode, respectively. A commercial potentiostat/galvanostat (Biologic SAS, model VSP 140) was used. In alkaline solutions, a calibrated commercial RHE (Hydroflex, Gaskatel) was employed. The catalyst film electrode is prepared as follows. The

homogenous catalysts ink can be firstly obtained through dispersing catalysts powder into the mixture of water, isopropanol and Nafion solution (5 wt%, Sigma-Aldrich) with the assistance of ultrasonic. Then the resultant ink was dropped on the surface of RRDE and dried in the oven at 60 °C for 10 min. The catalyst loading on the working electrode was fixed at 0.05 mg cm⁻². All measurements were repeated at least three times in order to ensure reproducibility.

Prior to the oxygen reduction measurement, successive cycle voltammetry (CV) was firstly performed to clean the Pt ring electrode in N₂-saturated 0.5 M H₂SO₄ electrolyte within the potential range from +0.05 to +1.2 V at a scan rate of 20 mV s⁻¹ until steady CVs were obtained. Then the background current (capacitive current) was collected by measuring CV in N₂-saturated electrolyte within the potential range from +1.1 to +0.05 V at a scan rate of 5 mV s⁻¹. After that, electrochemical impedance spectroscopy (EIS) was also carried out to measure the uncompensated resistance (R) of the liquid electrolyte for the subsequent iR-correction. iR correction values ranged from a few to a maximum of 15 mV. For the H-cell bulk electrolysis measurements, the uncompensated electrolyte resistance was corrected at the 85% level to ensure the stability of the electrochemical cell experiment, using the Manual IR compensation (MIR) technique (Biologic SAS EC Lab software). The remaining fraction of the IR correction was neglected. For all acid tests, the electrode potentials were converted to the reversible hydrogen electrode (RHE) according to the following equation:

$$E(RHE) = E(MMS) + 0.704 - iR \quad (3)$$

After purging with O₂ at least 30 min, the linear sweep voltammetry (LSV) was performed in O₂-saturated electrolyte within the potential range from +1.1 to +0.05 V at a scan rate of 5 mV s⁻¹ with the rotation speed of 1600 rpm. The faradaic currents on the disk electrode during the ORR process are obtained by subtraction of the corresponding capacitive current. The H₂O₂ amount produced at the disk electrode was evaluated by the ring current at a fixed ring potential of +1.2 V_{RHE}. The collection efficiency (N) of the ring electrode was 37%. The H₂O₂ selectivity (expressed as H₂O₂%, also referred to as the fraction of H₂O₂ produced) of the catalysts and the number of electrons transferred (n) were calculated according to the following equations^[59]:

$$H_2O_2 \% = 200 \times I_{ring} / ((N \times |I_{disk}| + I_{ring})) \quad (4)$$

$$n = 4|I_{disk}| / (|I_{disk}| + \frac{I_{ring}}{N}) \quad (5)$$

where I_{ring} is the positive ring current and I_{disk} is the negative disk current. Note that equation (4) reports H₂O₂ selectivity, and not efficiencies, because faradaic processes other than oxygen reduction are not taken into consideration.

Bulk H₂O₂ production was further evaluated by means of chronoamperometry at different applied working electrode potentials (+0.1, +0.2, and +0.3 V_{RHE}) in a custom-made two-chamber H-cell with a pre-treated Nafion® membrane as separator in acidic solution,^[13] anion exchange membrane (Selemion ASV, AGC Engineering Co., LTD) in neutral solution, and Selemion AHO in alkaline solution. The influences of different electrolytes (0.5 M H₂SO₄, 0.1 M K₂SO₄, and 0.1 M KOH) on H₂O₂ production were also investigated. UV-Vis photometric method was used to measure the produced H₂O₂ amount in regular time intervals. Sample solution aliquots were collected from the cathode compartment of the H-Cell and analysed using a commercial hydrogen peroxide test kits (Merck KGaA, Germany). The faradaic H₂O₂ efficiency (FE) was calculated from the H₂O₂ yield against the total quantity of charge passed:

$$H_2O_2 (FE, \%) = 2CVF/Q \quad (6)$$

where C is the H₂O₂ concentration (mol L⁻¹), V is the volume of electrolyte (L), F is the faraday constant (C mol⁻¹), Q is the passed charge amount (C). The passed charge amount can be obtained as the integral of current from t=0 to t=t (time of polarization at a given applied potential) according to the following equation: $Q = \int_0^t I(t, E_{\text{applied}}) dt$.

Acknowledgements

This work received funding by the German Federal Ministry of Education and Research (Bundesministerium für Bildung und Forschung, BMBF) under the grant 03SF0531B "HT-LINKED". ZELMI of Technical University Berlin is acknowledged for their support with TEM measurements. Yanyan Sun thanks China Scholarship Council (CSC) for the financial support.

Keywords: nitrogen-doped porous carbon • oxygen reduction • hydrogen peroxide production • bulk electrolysis • faradaic efficiency

- [1] D. Guo, R. Shibuya, C. Akiba, S. Saji, T. Kondo, J. Nakamura, *Science* **2016**, *351*, 361-365.
- [2] H. B. Yang, J. Miao, S. F. Hung, J. Chen, H. B. Tao, X. Wang, L. Zhang, R. Chen, J. Gao, H. M. Chen, L. Dai, B. Liu, *Sci. Adv.* **2016**, *2*, e1501122.
- [3] A. Zitolo, N. Ranjbar-Sahraie, T. Mineva, J. Li, Q. Jia, S. Stamatini, G. F. Harrington, S. M. Lyth, P. Kirtil, S. Mukerjee, E. Fonda, F. Jaouen, *Nat. Commun.* **2017**, *8*, 957.
- [4] A. Zitolo, V. Goellner, V. Armel, M. T. Sougrati, T. Mineva, L. Stievano, E. Fonda, F. Jaouen, *Nat. Mater.* **2015**, *14*, 937-942.
- [5] H. Fei, J. Dong, Y. Feng, C. S. Allen, C. Wan, B. Voloskiy, M. Li, Z. Zhao, Y. Wang, H. Sun, P. An, W. Chen, Z. Guo, C. Lee, D. Chen, I. Shakir, M. Liu, T. Hu, Y. Li, A. I. Kirkland, X. Duan, Y. Huang, *Nat. Catal.* **2018**, *1*, 63-72.
- [6] J. Wang, Z. Huang, W. Liu, C. Chang, H. Tang, Z. Li, W. Chen, C. Jia, T. Yao, S. Wei, Y. Wu, Y. Li, *J. Am. Chem. Soc.* **2017**, *139*, 17281-17284.
- [7] N. D. Leonard, S. Wagner, F. Luo, J. Steinberg, W. Ju, N. Weidler, H. Wang, U. I. Kramm, P. Strasser, *ACS Catal.* **2018**, *8*, 1640-1647.
- [8] X. Ge, A. Sumboja, D. Wu, T. An, B. Li, F. W. T. Goh, T. S. A. Hor, Y. Zong, Z. Liu, *ACS Catal.* **2015**, *5*, 4643-4667.
- [9] X. X. Wang, D. A. Cullen, Y. T. Pan, S. Hwang, M. Wang, Z. Feng, J. Wang, M. H. Engelhard, H. Zhang, Y. He, Y. Shao, D. Su, K. L. More, J. S. Spendelov, G. Wu, *Adv. Mater.* **2018**.
- [10] P. Song, M. Luo, X. Liu, W. Xing, W. Xu, Z. Jiang, L. Gu, *Adv. Funct. Mater.* **2017**, *27*, 1700802.
- [11] S. Li, C. Cheng, X. Zhao, J. Schmidt, A. Thomas, *Angew. Chem. Int. Ed.* **2018**, *57*, 1856-1862.
- [12] S. Li, C. Cheng, H. W. Liang, X. Feng, A. Thomas, *Adv. Mater.* **2017**, *29*.
- [13] Y. Y. Sun, I. Sinev, W. Ju, A. Bergmann, S. Dresch, S. Kuhl, C. Spori, H. Schmies, H. Wang, D. Bernsmeier, B. Paul, R. Schmack, R. Kraehnert, B. Roldan Cuenya, P. Strasser, *ACS Catal.* **2018**, *8*, 2844-2856.
- [14] S. Chen, Z. Chen, S. Siahrostami, T. R. Kim, D. Nordlund, D. Sokaras, S. Nowak, J. W. F. To, D. Higgins, R. Sinclair, J. K. Nørskov, T. F. Jaramillo, Z. Bao, *ACS Sustain. Chem. Eng.* **2017**, *6*, 311-317.
- [15] Z. Zheng, Y. H. Ng, D. W. Wang, R. Amal, *Adv. Mater.* **2016**, *28*, 9949-9955.
- [16] Y. Liu, X. Quan, X. Fan, H. Wang, S. Chen, *Angew. Chem. Int. Ed.* **2015**, *54*, 6837-6841.
- [17] S. Yang, J. Kim, Y. J. Tak, A. Soon, H. Lee, *Angew. Chem. Int. Ed.* **2016**, *55*, 2058-2062.
- [18] D. Iglesias, A. Giuliani, M. Melchionna, S. Marchesan, A. Criado, L. Nasi, M. Bevilacqua, C. Tavagnacco, F. Vizza, M. Prato, P. Fornasiero, *Chem* **2018**, *4*, 106-123.
- [19] W. P. Mounfield, A. Garg, Y. Shao-Horn, Y. Román-Leshkov, *Chem* **2018**, *4*, 18-19.
- [20] J. M. Campos-Martin, G. Blanco-Brieva, J. L. Fierro, *Angew. Chem. Int. Ed.* **2006**, *45*, 6962-6984.
- [21] C. Samanta, *Appl. Catal., A: Gen.* **2008**, *350*, 133-149.
- [22] A. Verdaguier-Casadevall, D. Deiana, M. Karamad, S. Siahrostami, P. Malacrida, T. W. Hansen, J. Rossmeisl, I. Chorkendorff, I. E. Stephens, *Nano Lett.* **2014**, *14*, 1603-1608.
- [23] J. S. Jirkovsky, I. Panas, E. Ahlberg, M. Halasa, S. Romani, D. J. Schiffrin, *J. Am. Chem. Soc.* **2011**, *133*, 19432-19441.
- [24] C. H. Choi, H. C. Kwon, S. Yook, H. Shin, H. Kim, M. Choi, *J. Phys. Chem. C* **2014**, *118*, 30063-30070.
- [25] S. Siahrostami, A. Verdaguier-Casadevall, M. Karamad, D. Deiana, P. Malacrida, B. Wickman, M. Escudero-Escribano, E. A. Paoli, R. Frydendal, T. W. Hansen, I. Chorkendorff, I. E. Stephens, J. Rossmeisl, *Nat. Mater.* **2013**, *12*, 1137-1143.
- [26] E. Pizzutilo, O. Kasian, C. H. Choi, S. Cherevko, G. J. Hutchings, K. J. J. Mayrhofer, S. J. Freakley, *Chem. Phys. Lett.* **2017**, *683*, 436-442.
- [27] C. H. Choi, M. Kim, H. C. Kwon, S. J. Cho, S. Yun, H. T. Kim, K. J. Mayrhofer, H. Kim, M. Choi, *Nat. Commun.* **2016**, *7*, 10922.
- [28] S. Siahrostami, M. E. Bjorketun, P. Strasser, J. Greeley, J. Rossmeisl, *Phys. Chem. Chem. Phys.* **2013**, *15*, 9326-9334.
- [29] X.-H. Yan, Z. Meng, J. Liu, T. Xue, *Mater. Lett.* **2018**, *217*, 171-173.
- [30] M. A. Ghanem, A. M. Al-Mayouf, M. N. Shaddad, F. Marken, *Electrochim. Acta* **2015**, *174*, 557-562.
- [31] W. R. P. Barros, Q. Wei, G. Zhang, S. Sun, M. R. V. Lanza, A. C. Tavares, *Electrochim. Acta* **2015**, *162*, 263-270.
- [32] F. Xu, T. Song, Y. Xu, Y. Chen, S. Zhu, S. Shen, *J. Rare Earths* **2009**, *27*, 128-133.
- [33] I. Yamanaka, S. Tazawa, T. Murayama, T. Iwasaki, S. Takenaka, *ChemSusChem* **2010**, *3*, 59-62.
- [34] I. Yamanaka, R. Ichihashi, T. Iwasaki, N. Nishimura, T. Murayama, W. Ueda, S. Takenaka, *Electrochim. Acta* **2013**, *108*, 321-329.
- [35] A. Bonakdarpour, D. Esau, H. Cheng, A. Wang, E. Gyenge, D. P. Wilkinson, *Electrochim. Acta* **2011**, *56*, 9074-9081.
- [36] K. Zhao, Y. Su, X. Quan, Y. Liu, S. Chen, H. Yu, *J. Catal.* **2018**, *357*, 118-126.
- [37] F. Hasché, M. Oezaslan, P. Strasser, T.-P. Fellinger, *J. Energy Chem.* **2016**, *25*, 251-257.
- [38] J. Park, Y. Nabae, T. Hayakawa, M.-a. Kakimoto, *ACS Catal.* **2014**, *4*, 3749-3754.
- [39] Y. Yang, F. He, Y. Shen, X. Chen, H. Mei, S. Liu, Y. Zhang, *Chem. Commun.* **2017**, *53*, 9994-9997.
- [40] Y.-H. Lee, F. Li, K.-H. Chang, C.-C. Hu, T. Ohsaka, *Appl. Catal. B: Environ.* **2012**, *126*, 208-214.
- [41] L. Qu, Y. Liu, J. B. Baek, L. Dai, *ACS Nano* **2010**, *4*, 1321-1326.
- [42] A. M. Abdelkader, D. J. Fray, *Nanoscale* **2017**, *9*, 14548-14557.
- [43] P. Perazzolo, C. Durante, R. Pilot, A. Paduano, J. Zheng, G. A. Rizzi, A. Martucci, G. Granozzi, A. Gennaro, *Carbon* **2015**, *95*, 949-963.
- [44] T. P. Fellinger, F. Hasche, P. Strasser, M. Antonietti, *J. Am. Chem. Soc.* **2012**, *134*, 4072-4075.
- [45] T. Xing, Y. Zheng, L. H. Li, B. C. Cowie, D. Gunzelmann, S. Z. Qiao, S. Huang, Y. Chen, *ACS Nano* **2014**, *8*, 6856-6862.
- [46] X. Liu, Y. Zhou, W. Zhou, L. Li, S. Huang, S. Chen, *Nanoscale* **2015**, *7*, 6136-6142.
- [47] Z. J. Han, C. Huang, S. S. Meysami, D. Piche, D. H. Seo, S. Pineda, A. T. Muddock, P. S. Bruce, P. S. Grant, N. Grobert, *Carbon* **2018**, *126*, 305-312.
- [48] R. Lv, Q. Li, A. R. Botello-Mendez, T. Hayashi, B. Wang, A. Berkdemir, Q. Hao, A. L. Elias, R. Cruz-Silva, H. R. Gutierrez, Y. A. Kim, H. Muramatsu, J. Zhu, M. Endo, H. Terrones, J. C. Charlier, M. Pan, M. Terrones, *Sci. Rep.* **2012**, *2*, 586.
- [49] T. Sharifi, G. Hu, X. Jia, T. Wagberg, *ACS Nano* **2012**, *6*, 8904-8912.
- [50] W. He, C. Jiang, J. Wang, L. Lu, *Angew. Chem. Int. Ed.* **2014**, *53*, 9503-9507.
- [51] W. Ju, A. Bagger, G. P. Hao, A. S. Varela, I. Sinev, V. Bon, B. Roldan Cuenya, S. Kaskel, J. Rossmeisl, P. Strasser, *Nat. Commun.* **2017**, *8*, 944.
- [52] A. S. Varela, W. Ju, P. Strasser, *Adv. Energy Mater.* **2018**, *1703614*.
- [53] F. V. E. dos Reis, V. S. Antonin, P. Hammer, M. C. Santos, P. H. C. Camargo, *J. Catal.* **2015**, *326*, 100-106.
- [54] J. Shui, C. Chen, L. Grabstanowicz, D. Zhao, D. J. Liu, *Proc. Natl. Acad. Sci.* **2015**, *112*, 10629-10634.
- [55] Z. Gong, G. Zhang, S. Wang, *J. Chem.* **2013**, *2013*, 1-9.
- [56] G. Yang, W. Choi, X. Pu, C. Yu, *Energy Environ. Sci.* **2015**, *8*, 1799-1807.
- [57] I. Kruusenberg, N. Alexeyeva, K. Tammeveski, *Carbon* **2009**, *47*, 651-658.
- [58] M. Scardamaglia, T. Susi, C. Struzzi, R. Snyders, G. Di Santo, L. Petaccia, C. Bittencourt, *Sci. Rep.* **2017**, *7*, 7960.

- [59] U. A. Paulus, T. J. Schmidt, H. A. Gasteiger, R. J. Behm, *J. Electroanal. Chem.* **2001**, 495, 134-145.

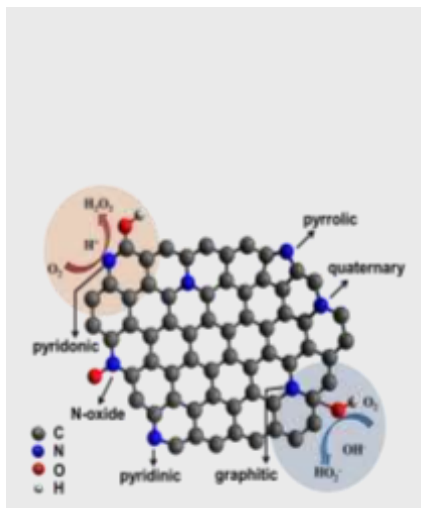
WILEY-VCH

Accepted Manuscript

Entry for the Table of Contents (Please choose one layout)

COMMUNICATION

Nitrogen-doped porous carbon catalysts were prepared using CMK-3 and polyethylenimine (PEI), exhibiting high H_2O_2 selectivity of 95.3% in acid, whereas large production rate of $570.1 \text{ mmol g}^{-1} \text{ catalyst h}^{-1}$ in neutral solution. Ex-situ X-ray photoemission spectroscopy analysis suggests a key mechanistic role of pyridinic-N in acid, while graphitic-N groups appear to be catalytically active moieties in neutral and alkaline conditions.



Yanyan Sun, Shuang Li, Zarko Jovanov, Huan Wang, Stefanie Kühn, and Peter Strasser*

Page No. – Page No.

Structure, activity, and faradaic efficiency of nitrogen-doped porous carbon catalysts for direct electrochemical hydrogen peroxide production

Accepted Manuscript